WILEY-VCH

Supporting Information

Counterintuitive Reversal of Circular Dichroism via Controllable Plasmonic Guided Mode Resonance in Diatomic Metasurfaces

Jiaqi Cheng, Zhancheng Li[*], Duk-Yong Choi, Wenwei Liu, Yuebian Zhang, Shiwang Yu, Hua Cheng[*], Jianguo Tian and Shuqi Chen[*]

Dr. J. Cheng, Dr. Z. Li, Dr. W. Liu, Dr. Y. Zhang, Dr. S. Yu, Prof. H. Cheng, Prof. J. Tian, Prof. S. Chen
The Key Laboratory of Weak Light Nonlinear Photonics, Ministry of Education, Ministry of Education, School of Physics and TEDA Institute of Applied Physics, Nankai University, Tianjin 300071, China
E-mail: zcli@nankai.edu.cn; hcheng@nankai.edu.cn; schen@nankai.edu.cn
Prof. D.-Y. Choi
Laser Physics Centre, Research School of Physics, Australian National University, Canberra, ACT, 2601, Australia
Prof. S. Chen
School of Materials Science and Engineering, Smart Sensing Interdisciplinary Science Center, Nankai University, Tianjin 300350, China
Prof. S. Chen
The Collaborative Innovation Center of Extreme Optics, Shanxi University, Taiyuan, Shanxi 030006, China

This file includes:

S1. *Chiroptical resonance of nanoresonators and the influence of variations in structural parameters on the chiroptical resonance of the designed diatomic metasurface*

S2. *Simulated reflection spectra of the designed metasurfaces with distinct spacing, and the analysis on the reason causing the difference between the simulated and measured reflection spectra*

S3. *Reflection spectra of the four designed coding elements for optical encryption*

S1. Chiroptical resonance of nanoresonators and the influence of variations in structural parameters on the chiroptical resonance of the designed diatomic metasurface

The designed diatomic metasurface is composed of two types of nanoresonators named A and B. The design of these chiral nanoresonators is indeed inspired by our previous research, as detailed in our publication (Adv. Mater. 2020, 32, 1907983).

The chiroptical resonances of the designed metasurface are attributed to planar intrinsic chirality. As shown in **Figure S1**, the spin-preserved reflection intensities r_{LR} and r_{RL} are equal and both close to zero. The circular dichroism (CD) is evidenced by the difference between the spin-flipped reflection intensities r_{RR} and r_{LL}, confirming that the CD originates from intrinsic planar chirality associated with polarization conversion. Additionally, the mirror image of the designed metasurface exhibits opposite chiroptical responses, wherein the spectra of LCP and RCP waves are exchanged and the CD signal reversed (Figure S1(b)).

To further validate that the chiroptical resonances at P_1 (1200 nm) and P_4 (1530 nm) in the designed metasurface correspond to surface lattice resonance (SLR) caused by the Wood-Rayleigh anomaly and plasmonic guided mode resonance (GMR), respectively, we simulated the variation of their resonant wavelengths and CD spectrum as the period of the metasurface along the x-direction (P_x) is altered. As illustrated in **Figure S2**, the resonant wavelengths of the chiroptical resonances at P_1 and P_4 exhibit a distinct redshift as P_x increases, consistent with theoretical predictions. Specifically, the SLR can be excited when the condition $\lambda \simeq n \times P$ (where λ is the resonant wavelength, n is the refractive index of the environment and P is the array period) is met, corresponding to the occurrence of the Wood-Rayleigh anomaly. In the simulation results, the wavelength of P_1 is nearly equal to P_x and varies linearly with P_x. The wave-vector matching condition for plasmonic GMR can be expressed as $\dfrac{2\pi n_{eff}}{\lambda} = \dfrac{2\pi m}{P_x} + k_x^m$,

where n_{eff} is the effective refractive index of the plasmonic guided mode, k_x^m is incident

wavevector, and m is number diffraction order. This linear relationship of the P_4 resonance wavelength with the structural period has also been confirmed in the simulated results. The field distribution in Figure 2(c) and the linear trend in Figure S2 confirm that P_1 corresponds to SLR and P_4 corresponds to GMR, where the resonance wavelengths are primarily determined by the periodicity of the metasurface. Furthermore, the sharp peak and abrupt change in the reflection spectra at P_1 (shown in Figure S1) also validate that the resonance is attributed to the Wood-Rayleigh anomaly. In contrast, the resonant wavelengths of resonances caused by the intrinsic properties of nanoresonators A and B show little change, as these resonances are governed by the intrinsic structural configuration of the nanoresonators themselves, independent of P_x. To further validate that the chiroptical resonances of the designed metasurface at P_2 (1250 nm) and P_3 (1370 nm) are attributed to the intrinsic resonance of nanoresonators A and B respectively, we simulated the absorption spectra of periodic metasurfaces individually composed of nanoresonators A and B. As shown in **Figure S3**, the absorption spectra of the periodic metasurface composed of nanoresonators A has an absorption peak around P_3, while that of the periodic metasurface composed of nanoresonators B displays an absorption peak around P_2. The result validates that the chiroptical response of the designed metasurface at P_3 and P_2 arises from the intrinsic resonance of nanoresonators A and B. The difference in resonance wavelengths between the designed metasurface and the periodic metasurfaces individually composed of nanoresonators A and B can be attributed to the near-neighbor interaction between the nanoresonators A and B in the designed metasurface.

The unique design of nanoresonators A and B is not only to showcase their individual chiroptical properties but, more importantly, to illustrate how nonlocal interactions can be leveraged to modulate the chiroptical response in a manner that transcends the individual chirality of the components. The chiroptical response of the designed metasurface at P_4 can be effectively tuned by adjusting the relative spacing (d) between the two types of nanoresonators, which is attributed to the modulation of the collective interference of the plasmonic GMRs.

Importantly, the collective interference of GMRs can be influenced not only by variations in d but also by changes in other structural parameters. We further analyze the variation of CD with the alteration of β_B, while maintaining $\beta_A = 80°$. As shown in **Figure S4,** the sign reversal of CD occurs when β_B changes. The peak of CD caused by the intrinsic resonance of nanoresonator B redly shifts with the increase of β_B. For $d = 500$ nm, CD is positive when $\beta_A \geq \beta_B$ and negative when $\beta_A < \beta_B$ at P_4. Conversely, for $d = 660$ nm, the situation is reversed. In comparison to the variations in CD resulting from changes in d, P_4 shows a more pronounced change with the variation in β_B. To achieve continuous manipulation of CD at a fixed operational wavelength, altering d is a more preferable choice.

Note that for a designed metasurface with $\beta_A = \beta_B = 80°$, sign reversal of CD can also be observed by adjusting d. Nevertheless, the range of CD variations is highly restricted, as shown in **Figure S5**. In this case, the GMR can still be excited under TE and TM illumination when d is not equal to $P_x/2$. However, the phase difference between guided mode fields excited by the TM and TE waves is close to 10 degrees and fixed with variations of d, while the resonant strength of GMRs enhanced with the increase of d. The sign reversal of CD is a result of competition between GMR and the low-Q chiroptical resonance at P_3. In order to realize continuous variation and counterintuitive reversal of CD around P_4, the structural parameters of the two nanoresonators in the unit cell of the designed metasurfaces have been carefully optimized.
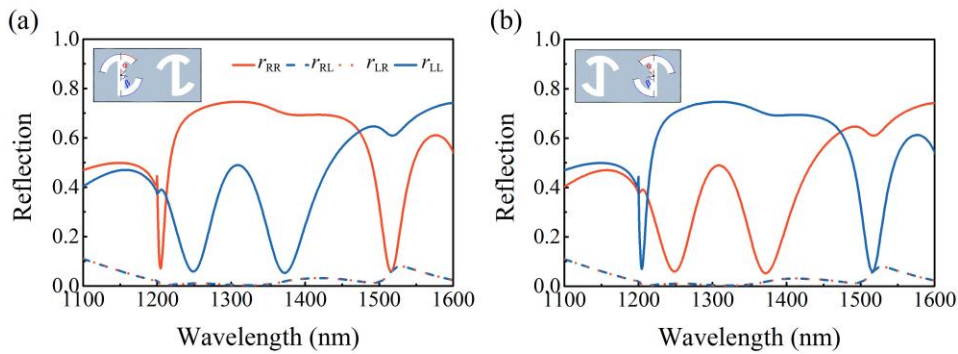
Figure S1. Simulated reflectance of different polarization components for the (a) proposed diatomic metasurfaces with $d = 500$ nm and (b) its mirror-symmetric structure.
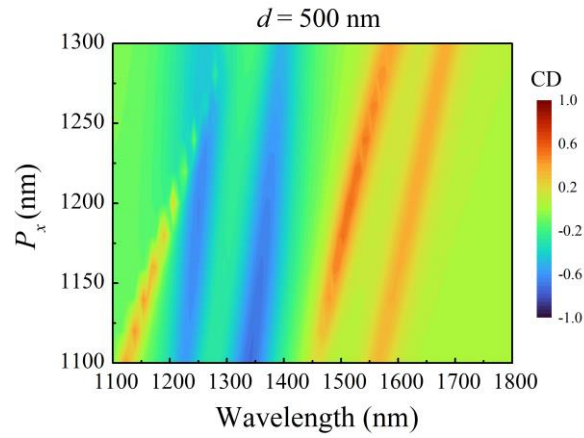

Figure S2. The variation of the value of CD and the corresponding resonant wavelengths of different chiroptical resonances in the designed metasurfaces with the change of x-directional period (P_x).
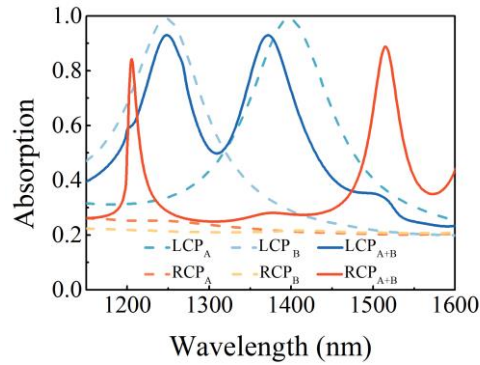

Figure S3. Simulated absorption spectra of the metasurfaces under LCP illumination and RCP illumination. Dashed lines show the results of periodic metasurfaces individually composed of nanoresonators A and B, and solid lines show the results of the designed diatomic metasurface with $d = 500$ nm. The blue colors indicate the results under LCP illumination, and the red colors indicate the results under RCP illumination.
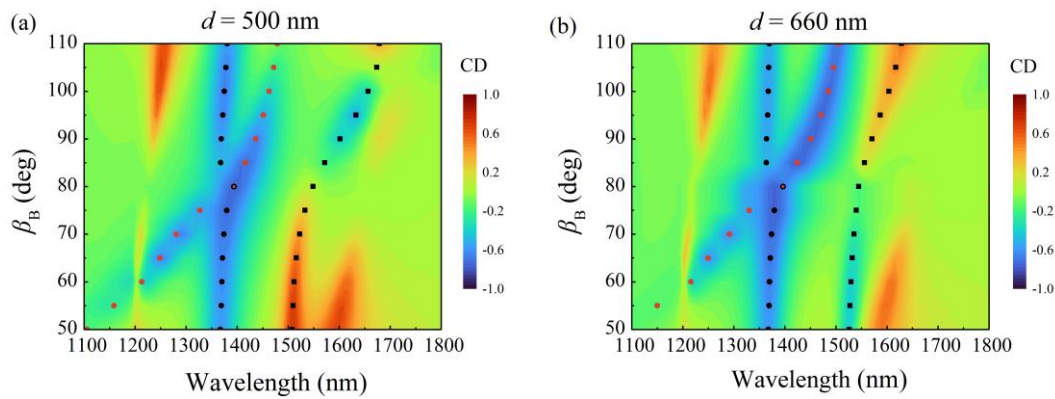
Figure S4. The variation of CD with the alteration of β_B for the diatomic metasurfaces with (a) $d = 500$ nm and (b) 660 nm. Trajectories marked with red circles represent the variation of chiroptical responses at P_2, those marked with black circles represent the changes in chiroptical responses at P_3, and those marked with black squares represent the variations in chiroptical responses at P_4.
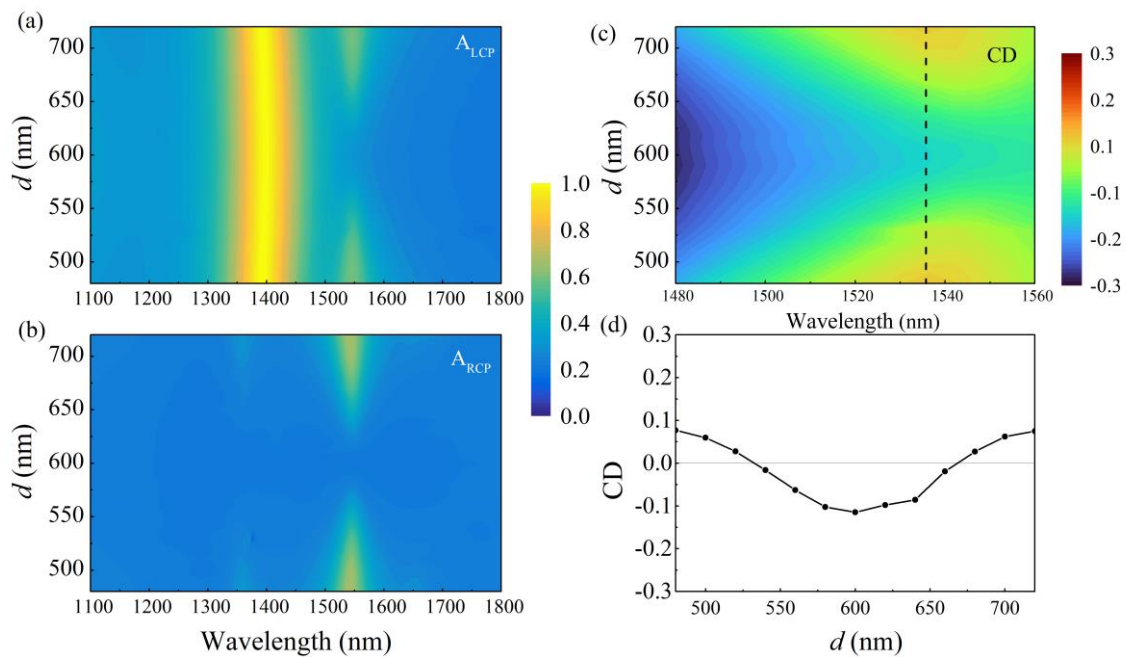

Figure S5. Absorption spectra of the designed metasurfaces composed of two identical nanoresonators under (a) LCP and (b) RCP illumination. (c) The variation of CD spectra with the changing of d and (d) the variation of CD at a fixed wavelength indicated by the black dash line in (c).

S2. Simulated reflection spectra of the designed metasurfaces with distinct spacing, and the analysis on the reason causing the difference between the simulated and measured reflection spectra

To make a comparison with the measured results, we simulated the reflection spectra of the designed diatomic metasurfaces with distinct d, as illustrated in **Figure S6**. The measured results are in good agreement with the simulated ones. The difference between the simulated and experimentally measured intensities, as well as the spectral linewidths at P_1 to P_4, can be attributed in part to the fabrication imperfections of the samples. Additionally, the differences arise from the fact that the simulated results were obtained under normal illumination conditions, whereas the measured results were acquired using objective-focused light. We simulated the reflection spectra of the designed metasurface with $d = 500$ nm under the oblique incidence of the LCP and RCP waves, as shown in **Figures S7**(a) and S7(b). The chiroptical resonance at P_1 under RCP illumination is highly dependent on the angle of incidence. The resonant peak can no longer be observed when the incident angle exceeds 2.5 degrees. Oblique incidence induces a red shift of the resonant peak at P_2 under LCP illumination and leads to an increase in the full width at half maximum (FWHM). The resonant strength at P_3 weakens as the incident angle increases. An increase in the oblique incident angle also results in a shift of the resonant wavelength at P_4 and a change in the resonant strength. The CD map is approximately symmetric about the $k_x = 0$ axis, as the chiroptical resonance originates from intrinsic planar chirality induced by structural anisotropy rather than extrinsic chirality resulting from oblique incidence. Figures S7(c) and S7(d) illustrate the calculated reflection spectra of the designed metasurface with $d = 500$ nm considering rough angle averaging. The incident angle values are calculated based on the numerical aperture (NA = 0.45) of the objective used in the experimental measurement for light focusing. The calculated results are in good agreement with the measured ones.
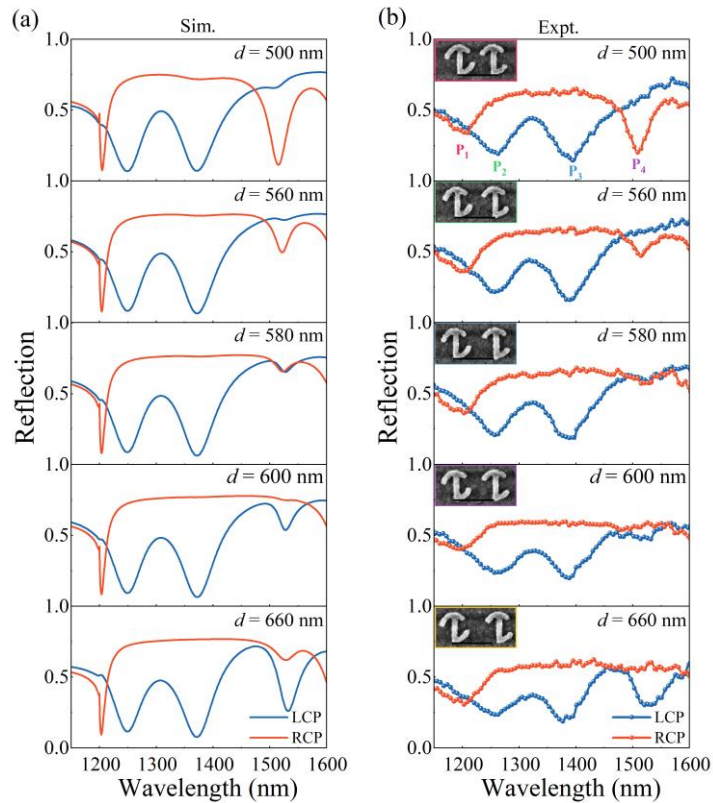
Figure S6. (a) Simulated and (b) measured reflection spectra of the designed metasurfaces with different *d* under LCP and RCP illuminations.
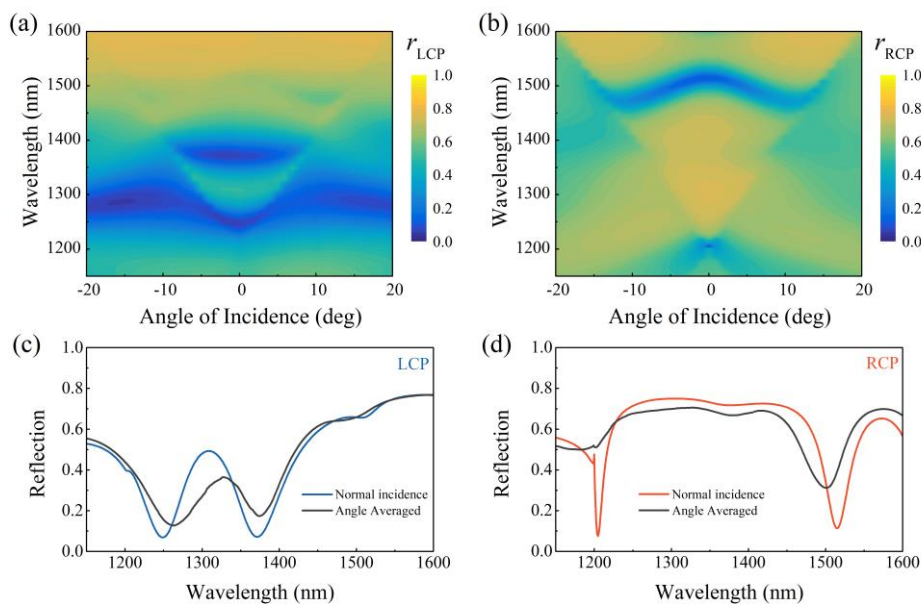

Figure S7. The variations in the reflected intensity of the designed metasurface with *d* = 500 nm as a function of the incident angle and wavelength under (a) LCP illumination and (b) RCP illumination. Simulated reflection spectra of the designed metasurface with *d* = 500 nm under (c) LCP and (d) RCP incidence with and without considering rough angle averaging.

S3. Reflection spectra of the four designed coding elements for optical encryption

Figure S8 shows the simulated reflection spectra of the four designed coding elements. Results indicate that the reflection spectra of the designed elements are nearly identical in the visible region and shows no chiroptical resonance. Under LCP illumination in the near-infrared region, element I shown no chiroptical resonance at P_3 due to the fact that it comprises two nanoresonators with the same structural parameters. The reflectance of elements II, III and IV differs only around P_4. Meanwhile, under RCP illumination in the near-infrared region, the reflection spectra of elements II, III and IV are almost the same, which is quite different from that of element I. Therefore, the element I and elements II to IV can be regarded as 2-bit coding elements "1" and "0" in the near-infrared region to achieve the binary grayscale image under both LCP and RCP illuminations. It can be found that the contrast of the binary grayscale image under RCP illumination is stronger than that under LCP illumination (Figure 4(e)), which is consistent with the simulated reflection spectra.
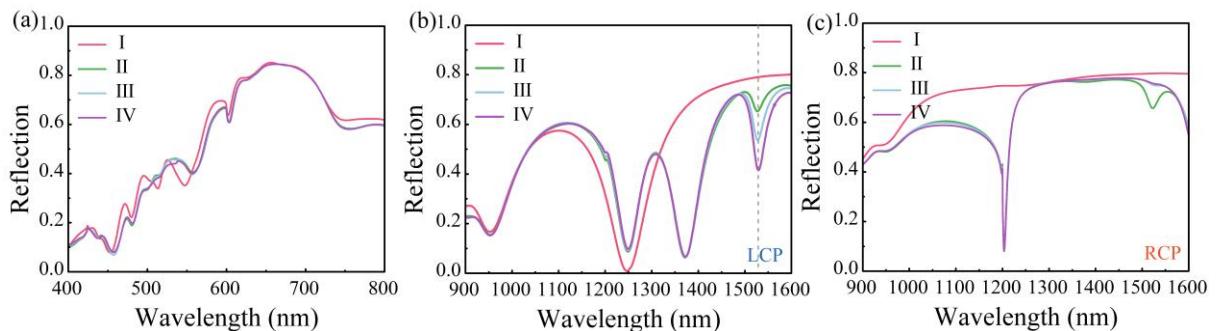

Figure S8. Reflection spectra of the four designed coding elements in (a) the visible region (under LCP/RCP illumination) and in the near-infrared region under (b) LCP and (c) RCP illumination.